Mitigating undersampling errors in MR fingerprinting by sequence optimization

Heesterbeek, David G.J.; Koolstra, Kirsten; van Osch, Matthias J.P.; van Gijzen, Martin B.; Vos, Franciscus M.; Nagtegaal, Martijn A.

DOI
10.1002/mrm.29554

Publication date
2022

Document Version
Final published version

Published in
Magnetic Resonance in Medicine

Received: 18 July 2022 | Revised: 11 November 2022 | Accepted: 19 November 2022

DOI: 10.1002/mrm.29554

RESEARCH ARTICLE

Magnetic Resonance in Medicine

Mitigating undersampling errors in MR fingerprinting by sequence optimization

David G.J. Heesterbeek[1,2] | **Kirsten Koolstra**[3] | **Matthias J.P. van Osch**[4] | **Martin B. van Gijzen**[2] | **Franciscus M. Vos**[1,5] | **Martijn A. Nagtegaal**[1,4]

[1]Department of Imaging Physics, Delft University of Technology, Delft, The Netherlands

[2]Delft Institute of Applied Mathematics, Delft University of Technology, Delft, The Netherlands

[3]LKEB of the Department of Radiology, Leiden University Medical Center, Leiden, The Netherlands

[4]C.J. Gorter MRI center of the Department of Radiology, Leiden University Medical Center, Leiden, The Netherlands

[5]Department of Radiology, Erasmus University Medical Center, Rotterdam, The Netherlands

Correspondence
David G.J. Heesterbeek, Department of Radiotherapy, University Medical Center Utrecht, Heidelberglaan 100, 3584 CX, Utrecht, The Netherlands.
Email: D.G.J.Heesterbeek-4@umcutrecht.nl

Funding information
Medical Delta: Dementia and Stroke, Grant/Award Number: 3.0

Purpose: To develop a method for MR Fingerprinting (MRF) sequence optimization that takes both the applied undersampling pattern and a realistic reference map into account.

Methods: A predictive model for the undersampling error leveraging on perturbation theory was exploited to optimize the MRF flip angle sequence for improved robustness against undersampling artifacts. In this framework parameter maps from a previously acquired MRF scan were used as reference. Sequences were optimized for different sequence lengths, smoothness constraints and undersampling factors. Numerical simulations and in vivo measurements in eight healthy subjects were performed to assess the effect of the performed optimization. The optimized MRF sequences were compared to a conventionally shaped flip angle pattern and an optimized pattern based on the Cramér–Rao lower bound (CRB).

Results: Numerical simulations and in vivo results demonstrate that the undersampling errors can be suppressed by flip angle optimization. Analysis of the in vivo results show that a sequence optimized for improved robustness against undersampling with a flip angle train of length 400 yielded significantly lower median absolute errors in T_1: 5.6% ± 2.9% and T_2: 7.9% ± 2.3% compared to the conventional (T_1: 8.0% ± 1.9%, T_2: 14.5% ± 2.6%) and CRB-based (T_1: 21.6% ± 4.1%, T_2: 31.4% ± 4.4%) sequences.

Conclusion: The proposed method is able to optimize the MRF flip angle pattern such that significant mitigation of the artifacts from strong k-space undersampling in MRF is achieved.

KEYWORDS
MR fingerprinting, optimal experiment design, quantitative MRI, undersampling

1 | INTRODUCTION

MR fingerprinting (MRF) samples the MR signal in a transient-state while varying acquisition parameters are applied.[1] After each excitation pulse an undersampled k-space read-out is acquired and reconstructed by zero-filling, even though this results in severe aliasing artifacts. Tissue parameters are generally estimated using inner product matching of the measured signal to a precalculated dictionary (e.g. yielding the longitudinal relaxation time T_1, transverse relaxation time T_2 and magnitude of the steady-state magnetization ρ or M_0).

Sequence optimization has been performed to increase the accuracy of the parameter maps and to further reduce the scan time.[2] Most previous methods for sequence optimization modeled the errors in the MRF signal as independent, zero-mean stochastic noise.[3-7] However, these approaches neglected spatial correlations between voxels introduced by the undersampling. For shorter acquisition times, either due to high undersampling factor and/or low number of time indices, the undersampling error can have a large effect on the accuracy and the image quality of the parameter maps.[8]

In recent work, Jordan et al.[9] proposed an MRF-sequence optimization scheme that explicitly models undersampling effects as well as spatial variations of the signal phase, potentially caused by spatial variations in the B_0 and B_1 field. To reduce the computational complexity, a reference image was separated into white matter, gray matter and CSF fractions using three reference T_1, T_2 combinations. For each tissue type undersampling artifacts were precalculated per time point using the respective fraction maps. During iterations of the optimization scheme only the transverse magnetization of the three tissue types was recalculated and used as weighting per time point to obtain time-frame images. Based on these simplified reference maps, error estimates could be obtained, thereby allowing an iterative optimization procedure to reduce undersampling errors.

In this paper we aim to develop a new MRF optimization method to mitigate undersampling artifacts that applies a more sophisticated spatial reference map. While doing so, our focus will be on the flip angle train. To overcome the issue of high computational complexity we use a recently proposed model relying on perturbation theory, to predict the interplay between a specific MRF acquisition scheme and the undersampling artifacts in the tissue parameter maps.[8] Our method does not require the calculation of extensive MRF-dictionaries, includes the spatially varying signal phase in the model and allows to use any reference parameter map as target for the optimization. The predictive model and optimized sequences will be validated by means of simulations and in vivo brain scans. We hypothesize that optimization of the flip angle train can significantly reduce the undersampling errors in the reconstructed parameter maps.

2 | THEORY

To provide the necessary background for the performed optimization and context to the presented results, the MRF-undersampling model proposed by Stolk and Sbrizzi[8] is briefly described. We will use this model for sequence optimization in Section 3. Essentially, the model gives an analytical expression for the estimated quantitative parameter maps $\boldsymbol{\theta}^*$ resulting from an MRF experiment:

$$\boldsymbol{\theta}^* \approx \boldsymbol{\theta} + \mathrm{PSFE}(\boldsymbol{\theta}) + \mathcal{E}_1(\boldsymbol{\alpha}) + \mathcal{E}_2(\boldsymbol{\theta};\boldsymbol{\alpha}), \tag{1}$$

in which $\boldsymbol{\theta} \in \mathbb{R}^{N_\theta \times N_I \times N_I}$ are the N_θ reference tissue parameter maps of $N_I \times N_I$ voxels; $\boldsymbol{\alpha}$ represents the flip angle pattern and PSFE is the point spread function error that depends on the k-space sampling pattern, but is independent of the flip angle pattern (only minimized by adjusting the undersampling scheme). Importantly, $\mathcal{E}_1(\boldsymbol{\alpha})$ and $\mathcal{E}_2(\boldsymbol{\theta};\boldsymbol{\alpha})$ are error terms that do depend on the flip angle pattern and can therefor be minimized by appropriately adjusting the flip angles. In further equations the dependence on $\boldsymbol{\alpha}$ has been omitted for ease of notation.

The (to be estimated) parameters of our focus are: $\boldsymbol{\theta}^{(*)}(\vec{x}) = \left(T_1^{(*)}(\vec{x}), T_2^{(*)}(\vec{x}), \mathrm{Re}\{\rho^{(*)}(\vec{x})\}, \mathrm{Im}\{\rho^{(*)}(\vec{x})\}\right)^T$ such that the number of parameters $N_\theta = 4$. Notice that the steady state magnetization $\rho^{(*)} \in \mathbb{C}^{N_I \times N_I}$ contains the (estimated) spatially varying, signal phase.

The rest of this section contains an overview of the key steps in the model derivation from Stolk et al.[8] The undersampled time-series images from an MRF scan are written as a convolution of the transverse magnetization at time TE of the readout with a Point Spread Function (PSF) that depends on the k-space sampling scheme:

$$I_j(\vec{x}|\boldsymbol{\theta}) = \sum_{\vec{y} \in G} P_j(\vec{x} - \vec{y})\, m_j(\boldsymbol{\theta}(\vec{y})), \tag{2}$$

in which $I_j(\vec{x}|\boldsymbol{\theta}) \in \mathbb{C}^{N_I \times N_I}$ is the undersampled time-series image at time index j; G is the spatial domain; $P_j \in \mathbb{C}^{(N_I + 2\lfloor N_I/2 \rfloor) \times (N_I + 2\lfloor N_I/2 \rfloor)}$ is the PSF for time index j that models the effect of undersampling; $\boldsymbol{m}(\boldsymbol{\theta}) \in \mathbb{C}^{N_J}$ is the transverse magnetization over time determined by reference parameters $\boldsymbol{\theta}$ and $m_j(\boldsymbol{\theta})$ the magnetization at time index j.

Observe that (2) partitions the description of the undersampled images in a spatial component (the PSF) that depends on the k-space sampling pattern, and a temporal

component (the transverse magnetization) that depends on the flip angle pattern. Only the temporal component needs to be updated when optimizing for the acquisition parameters. This proves to be useful for obtaining feasible calculation times.

MRF parameter estimation can be conceived as the voxel-wise least-square minimization based on N_J time-series images $\boldsymbol{I} \in \mathbb{C}^{N_J \times N_I \times N_I}$:

$$\boldsymbol{\theta}^*(\vec{x}) = \underset{\tilde{\boldsymbol{\theta}} \in \mathbb{R}^{N_\theta}}{\arg\min} \left\| \boldsymbol{I}(\vec{x}|\boldsymbol{\theta}) - \boldsymbol{m}(\tilde{\boldsymbol{\theta}}) \right\|^2, \tag{3}$$

in which $\boldsymbol{I}(\vec{x}|\boldsymbol{\theta}) \in \mathbb{C}^{N_J}$ denotes the observed signal in a voxel at location $\vec{x}$, which depends on $\boldsymbol{\theta}$ in all voxels due to the applied PSF.

The estimate $\boldsymbol{\theta}^*$ is a stationary point of the objective function (3), such that:

$$\mathrm{Re}\left\{ \left\langle \left(\boldsymbol{m}(\tilde{\boldsymbol{\theta}}) - \boldsymbol{I}(\vec{x}|\boldsymbol{\theta}) \right), \frac{\partial}{\partial \theta_p} \boldsymbol{m}(\tilde{\boldsymbol{\theta}}) \right\rangle \right\} \Bigg|_{\tilde{\boldsymbol{\theta}} = \boldsymbol{\theta}^*(\vec{x})} = 0, \tag{4}$$

for all $\vec{x}$ in the spatial domain G and each $p \in \{1, 2, .., N_\theta\}$.

From (2) and (4) it can be deduced that:

$$0 = \mathrm{Re}\left\{ \sum_{j=1}^{N_J} m_j\left(\boldsymbol{\theta}^*(\vec{x})\right) \overline{\mathcal{D}m_{j;p}\left(\boldsymbol{\theta}^*(\vec{x})\right)} - \sum_{j=1}^{N_J} \sum_{\vec{y} \in G} P_j(\vec{x} - \vec{y})\, m_j\left(\boldsymbol{\theta}(\vec{y})\right) \overline{\mathcal{D}m_{j;p}\left(\boldsymbol{\theta}^*(\vec{x})\right)} \right\}, \tag{5}$$

in which $\overline{\mathcal{D}\boldsymbol{m}}$ is the complex conjugate of the Jacobian matrix of the magnetization vector $\boldsymbol{m}$.

Since (5) cannot be rewritten in a closed form expression for $\boldsymbol{\theta}^*$, a perturbation theoretic expansion is initially performed which is subsequently linearized. It is assumed that the range of tissue parameter values is small such that the magnetization can be considered linear with respect to the tissue parameters, allowing for the expansion. Defining $\boldsymbol{\eta} = (T_1, T_2)$, the parameters of $\boldsymbol{\theta}$ and $\boldsymbol{\theta}^*$ are expanded through:

$$\begin{aligned} \boldsymbol{\eta}^{(*)}(\vec{x}) &= \boldsymbol{\eta}_0 + \boldsymbol{\eta}_1^{(*)}(\vec{x}), \\ \rho^{(*)}(\vec{x}) &= \rho_0^{(*)}(\vec{x}) \left(1 + \rho_1^{(*)}(\vec{x})\right), \end{aligned} \tag{6}$$

in which $\boldsymbol{\eta}_0$ are the assumed spatially constant values that we set to the mean T_1 and T_2 value of the reference map; $\boldsymbol{\eta}_1^{(*)}(\vec{x})$ and $\rho_1^{(*)}(\vec{x})$ are (estimated) contrast terms (i.e. offsets with respect to constants) and ρ_0 is a binary mask for zero-signal areas. Due to the linearity of $\rho^{(*)}$ in the magnetization function we can write:

$$\boldsymbol{m}\left(\boldsymbol{\theta}^{(*)}(\vec{x})\right) = \rho_0^{(*)}(\vec{x})\, \boldsymbol{m}\left(\boldsymbol{\theta}_0 + \boldsymbol{\theta}_1^{(*)}(\vec{x})\right), \tag{7}$$

in which

$$\rho_0^*(\cdot) = \frac{1}{N_J} \sum_{j=1}^{N_J} P_j(\cdot) * \rho_0(\cdot) \tag{8}$$

and

$$\begin{aligned} \boldsymbol{\theta}_0 + \boldsymbol{\theta}_1^{(*)}(\vec{x}) &= (\boldsymbol{\eta}_0, 1, 0)^T \\ &+ \left(\boldsymbol{\eta}_1^{(*)}(\vec{x}), \mathrm{Re}\left\{ \rho_1^{(*)}(\vec{x}) \right\}, \mathrm{Im}\left\{ \rho_1^{(*)}(\vec{x}) \right\} \right)^T. \end{aligned} \tag{9}$$

Note that because of the binary mask $\boldsymbol{\theta}^{(*)}(\vec{x}) \neq \boldsymbol{\theta}_0 + \boldsymbol{\theta}_1^{(*)}(\vec{x})$.

The perturbation equations (6) and (9) facilitate extraction of an explicit expression for $\boldsymbol{\theta}^*(\vec{x})$. This is done by substituting the perturbation theoretic expansions and performing a first-order Taylor expansion of the two terms in (5) around $\boldsymbol{\theta}_0$. For instance, the Taylor expansion of the first term in (5) yields:

$$\begin{aligned} & m_j\left(\boldsymbol{\theta}^*(\vec{x})\right) \overline{\mathcal{D}m_{j;p}\left(\boldsymbol{\theta}^*(\vec{x})\right)} = \\ & \left|\rho_0^*(\vec{x})\right|^2 \cdot m_j\left(\boldsymbol{\theta}_0 + \boldsymbol{\theta}_1^*(\vec{x})\right) \overline{\mathcal{D}m_{j;p}\left(\boldsymbol{\theta}_0 + \boldsymbol{\theta}_1^*(\vec{x})\right)} \approx \\ & \left|\rho_0^*(\vec{x})\right|^2 \cdot \left(m_j(\boldsymbol{\theta}_0) \overline{\mathcal{D}m_{j;p}(\boldsymbol{\theta}_0)} + \sum_{q=1}^{N_\theta} \mathcal{D}m_{j;q}(\boldsymbol{\theta}_0) \overline{\mathcal{D}m_{j;p}(\boldsymbol{\theta}_0)} \theta_{1,q}^*(\vec{x}) \right) \\ & + \sum_{q=1}^{N_\theta} m_j(\boldsymbol{\theta}_0) \overline{\mathcal{D}^2 m_{j;p,q}(\boldsymbol{\theta}_0)} \theta_{1,q}^*(\vec{x}) \Bigg). \end{aligned} \tag{10}$$

Based on these Taylor expansions an *explicit* expression for $\boldsymbol{\theta}_1^*(\vec{x})$ can be obtained, that can be rewritten into the form presented in Equation (1). For the error terms $\mathcal{E}_1$ and $\mathcal{E}_2$ this results in:

$$\begin{aligned} \mathcal{E}_{1;p}(\boldsymbol{\alpha}) &= \left|\rho_0^*\right|^2 \sum_{q=1}^{N_\theta} \mathrm{Re}\{N\}_{p,q}^{-1} \mathrm{Re}\left\{ \overline{\rho_0^*} S_{\mathrm{resid;q}}^{(1,0)} * \rho_0 \right\}, \\ \mathcal{E}_{2;p}(\boldsymbol{\theta}, \boldsymbol{\alpha}) &= \left|\rho_0^*\right|^2 \sum_{q=1}^{N_\theta} \mathrm{Re}\{N\}_{p,q}^{-1} \mathrm{Re}\left\{ \overline{\rho_0^*} \sum_{r=1}^{N_\theta} S_{\mathrm{resid;q,r}}^{(1,1)} * \left(\rho_0 \theta_{1;r}\right) \right\}, \end{aligned} \tag{11}$$

for $p \in \{1, 2, .., N_\theta\}$. Here the following definitions have been used:

$$\begin{aligned} N_{p,q} &= \sum_{j=1}^{N_J} \overline{\mathcal{D}m_{j;p}(\boldsymbol{\theta}_0)} \mathcal{D}m_{j;q}(\boldsymbol{\theta}_0), \\ S_{\mathrm{resid;q}}^{(1,0)} &= \sum_{j=1}^{N_J} \left(P_j - \frac{1}{N_J} \sum_{i=1}^{N_J} P_i \right) \overline{\mathcal{D}m_{j;q}(\boldsymbol{\theta}_0)} m_j(\boldsymbol{\theta}_0), \\ S_{\mathrm{resid;q,r}}^{(1,1)} &= \sum_{j=1}^{N_J} \left(P_j - \frac{1}{N_J} \sum_{i=1}^{N_J} P_i \right) \overline{\mathcal{D}m_{j;q}(\boldsymbol{\theta}_0)} \mathcal{D}m_{j;r}(\boldsymbol{\theta}_0). \end{aligned} \tag{12}$$

Note that N is also known as the Fisher information matrix. A more detailed derivation of (1) can be found in for example Stolk et al.[8,10] Using this approach, an expression is found for the predicted parameters (given

certain reference parameter values). We will use this expression to mitigate the undersampling dependent error terms.

One may observe that the derived expression for $\boldsymbol{\theta}_1^*$ only depends on $\boldsymbol{m}(\boldsymbol{\theta}_0)$ and the first- and second-order derivatives of $\boldsymbol{m}$ in $\boldsymbol{\theta}_0$. Next to the use of precomputed PSFs (see (2)), this is the second step that makes this model suitable for sequence optimization, since only $\boldsymbol{m}(\boldsymbol{\theta}_0)$ and its derivatives are required instead of the computation of a large dictionary.

3 | METHODS

Methods were implemented in Python. The full implementation of the proposed optimization scheme, used reference maps and optimized sequences can be found at https://github.com/imphys/MRF_undersampling_optimization.[11] Results were visualized with Python libraries Matplotlib[12] and Seaborn.[13]

3.1 | Sequence optimization

MRF sequences were optimized for a gradient spoiled steady-state free precession acquisition[14] with a fixed repetition time of 15 ms. The Extended Phase Graph formalism[15] was used to simulate the MRF signals $\boldsymbol{m}(\boldsymbol{\theta})$ over time. Using this approach the derivatives with respect to the tissue parameters can be calculated analytically through differentiation of the relaxation matrix and the term representing the recovery toward thermal equilibrium. All MRF scans used the same constant density, spiral k-space trajectory with an effective undersampling factor of 1/32. Incremental steps of 360°/32 rotation were applied between readouts and starting angles were equally distributed across sequence repetitions.

The cost function for this optimization problem was based on the relative errors $r_{\{1,2\},i}$ predicted by the model:

$$r_{\{1,2\},i} = \frac{T^{\text{und}}_{\{1,2\},i} - T^{\text{ref}}_{\{1,2\},i}}{T^{\text{ref}}_{\{1,2\},i}}, \tag{13}$$

for voxel i where $\text{T}^{\text{und}}_{\{1,2\},i}$ denotes the (undersampled) predictions resulting from (1) and $\text{T}^{\text{ref}}_{\{1,2\},i}$ is the reference value. The Root-Mean-Square (RMS) of the relative errors of nonmasked voxels was used as a measure for the optimization performance:

$$\text{RMS}_{T_{\{1,2\}}} = \sqrt{\frac{1}{N_{\text{vox}}}\sum_{i=1}^{N_{\text{vox}}} r^2_{\{1,2\},i}}, \tag{14}$$

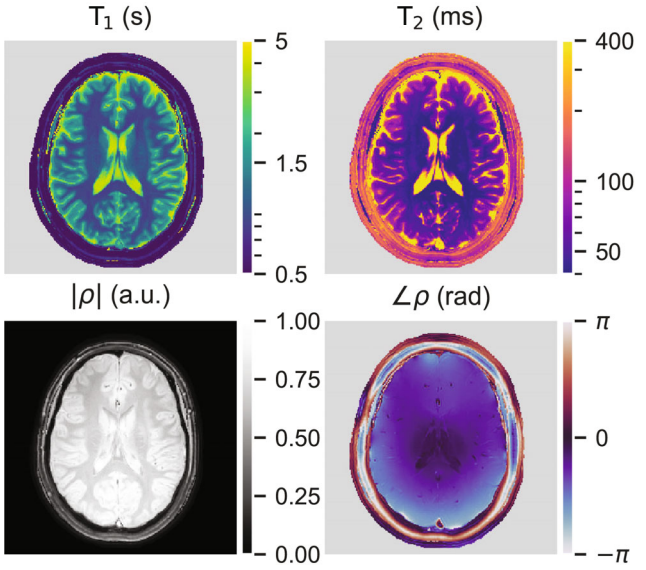

FIGURE 1 Maps of T_1, T_2, and ρ that were used as reference in sequence optimizations for the in vivo data. Maps were estimated from a previously performed fully sampled 3 T inversion recovery gradient spoiled steady-state free precession MR fingerprinting acquisition.

in which N_{vox} is the number of nonmasked voxels. The mask used to calculate the RMS error strictly removed the zero-signal voxels (air) surrounding the head. Optimizations for in vivo data were based on previously acquired parameter maps from a single, fully sampled brain slice masked by thresholding the proton density map (see Figure 1).

Different optimization schemes were considered. Mathematically this design problem was posed as:

$$\begin{aligned} \min_{\{\alpha_j\}_{j=1}^{N_J}} \quad & \text{Cost function} \\ \text{s.t.} \quad & ① : \text{LB} \le \alpha_1 \le 180° \\ & \text{LB} \le \alpha_j \le 60° \qquad \forall\, j \in \{2,3,..,N_J\} \\ & ② : |\alpha_{j+1} - \alpha_j| \le 1° \quad \forall\, j \in \{2,3,\ \dots\ ,N_J - 1\}, \end{aligned} \tag{15}$$

in which the cost function is dependent on the relative errors while LB is a to be defined Lower Bound, as presented in Table 1. The (six) performed optimizations were variations on the first optimization option *OptA*, with $\frac{1}{2}\left(\text{RMS}_{T_1} + \text{RMS}_{T_2}\right)$ as cost function, using 400 flip angles, a 1/32 undersampling factor, a 10° lower bound and a smoothness constraint. We performed the variations (see Table 1) to study the effects of the applied constraints. The first constraint was introduced to restrict the solution space and limit power deposition. The second constraint, on the flip angle difference, promotes a smooth evolution of the transverse magnetization. These constraints

TABLE 1 Settings for the optimizations as performed in this study

Name	Cost function	Sequence length (N_J)	Undersampling factor	Readouts	Lower Bound constraint ①	Smoothness constraint ②
Optimization A (*OptA*)	$\frac{1}{2}(\mathrm{RMS}_{T_1} + \mathrm{RMS}_{T_2})$	400	1/32	400	10°	✓
Optimization B (*OptB*)	$\frac{1}{2}(\mathrm{RMS}_{T_1} + \mathrm{RMS}_{T_2})$	400	3/32	1200	10°	✓
Optimization C (*OptC*)	$\frac{1}{2}(\mathrm{RMS}_{T_1} + \mathrm{RMS}_{T_2})$	200	2/32	400	10°	✓
Optimization D (*OptD*)	$\frac{1}{2}(\mathrm{RMS}_{T_1} + \mathrm{RMS}_{T_2})$	400	1/32	400	0°	✓
Optimization E (*OptE*)	$\frac{1}{2}(\mathrm{RMS}_{T_1} + \mathrm{RMS}_{T_2})$	400	1/32	400	10°	×
Optimization F (*OptF*)	RMS_{T_2}	400	1/32	400	10°	✓

were similar to Zhao et al.[5] A conventionally shaped MRF sequence (see Figure 4) was used as initialization in all optimizations.

We solved the optimization problem (15) using Sequential Least-Square Quadratic Programming.[16] This algorithm reformulates the problem by applying a quadratic approximation to the cost function at the current solution. The resulting constrained, quadratic optimization problem is solved based on a linearization of the constraints. Since the problem is nonconvex, global convergence is not guaranteed and the algorithm can get stuck in a poor local minimum. However, in initial experiments we did not observe this behavior.

A multiprocessor implementation with eight CPUs (Intel E5-2683 CPU) was used to compute the different gradient steps in the Sequential Least-Square Quadratic Programming algorithm. This resulted in calculation times of approximately 32 h per complete sequence optimization during which 400 parameters were optimized.

Our optimized sequences were compared to a state-of-the-art optimization method based on the Cramér–Rao lower bound (CRB).[5] The CRB is a theoretical lower bound on the variance of any unbiased estimator of parameters assuming stochastic noise. The normalized CRB for a single tissue voxel was calculated as $\mathrm{nCRB}(\theta_p) = \sqrt{\frac{\rho^2 \mathrm{CRB}(\theta_p)}{\theta_p^2 \sigma^2}}$ for tissue parameter θ_p, where ρ is the steady-state magnetization and σ^2 is the variance of the stochastic noise. Using the Sequential Least-Square Quadratic Programming solver, a sequence with minimal nCRB for an a priori defined set of tissues was obtained. Two single tissue signals with representative values for white and gray matter in the brain were chosen for the optimization, that is, $(T_1, T_2) = (700\ \mathrm{ms}, 60\ \mathrm{ms}), (1100\ \mathrm{ms}, 100\ \mathrm{ms})$ from Zhao et al.,[5] while the constraints of *OptA* (see Table 1) were used. The normalized CRB values were also calculated for the optimized sequences as previously proposed (*OptA-F*). For this purpose, 1000 T_1 and T_2 combinations were randomly drawn from the reference maps as shown in Figure 1.

3.2 | Numerical experiments

A numerical checkerboard phantom was used for validation of the error model and our optimization strategy. Furthermore, it was used to study the effect of spatial variations in the signal phase, which was modeled as a time-wise constant complex phase term, while applying a conventionally shaped FA-pattern. The MRF-undersampling model proposed by Stolk and Sbrizzi[8] was validated by comparison to brute force simulations. They consisted of Extended Phase Graph simulations, subsequently Fourier transformation, undersampling and then inverse (nonuniform) Fourier transformed image formation, after which parameter estimates were obtained via dictionary matching. The efficacy of our optimization strategy was tested using the numerical phantom as reference map and with constraints as for *OptA* (see Table 1).

3.3 | In vivo experiments

In vivo brain scans were acquired on a 3.0 T Philips Ingenia MRI scanner (Philips, Best, The Netherlands) from eight healthy subjects to compare the performance of the different MRF sequences. This study was approved by the local medical ethics committee and from all volunteers informed consent was obtained prior to image acquisition. Subjects were instructed to move as little as possible during the entire scan session.

In each subject, the conventional sequence (*Conv*), *OptA*, and the CRB optimized sequence were all acquired with the undersampling factors 1/32, 3/32 and 32/32 (fully sampled). These fully sampled acquisitions essentially resulted in three reference maps for each subject. Sequence

OptB was acquired with an undersampling factor of 3/32, *OptC* with 2/32 and *OptD-F* with 1/32. A delay time of 6 s was used between repetitions of the same flip angle patterns. Two slices were acquired with a 2-cm slice gap of which the lower slice was positioned to intersect the ventricles, similar to Figure 1. The field of view was 224×224 mm^2 with a resolution of 1×1 mm^{2}and 5 mm slice thickness.

A dictionary was calculated for each flip angle pattern with T_1 values ranging from 150 ms to 5 s and T_2 values from 30 ms to 1 s both applying a step size of 3%. Dictionary matching was performed to obtain ρ, T_1 and T_2 estimates. To minimize errors due to slight motion, the fully sampled reference scans and undersampled scans were rigidly registered based on the T_1 maps using the mutual information metric.[17] After registration, voxel-wise relative error maps $\mathbf{r}_{1,2}$ (13) were computed for each undersampled acquisition based on the three different fully sampled reference series. Using the parameter maps, brain tissue was segmented by applying a signal intensity threshold to exclude regions outside the skull and a $T_1 > 1.6$ s threshold to exclude CSF to prevent unpredictable errors due to flow phenomena. From the masked relative error maps, the median absolute (relative) error was calculated:

$$\mathrm{MAE}_{\{1,2\}} = \mathrm{median}\left(\left|\mathbf{r}_{\{1,2\}}\right|\right). \tag{16}$$

This was found to be a more robust error measure compared to the RMSE which is sensitive to outliers. Note that the mask applied to calculate the MAE and generate the figures in the results is different from the one applied to calculate the RMSE used for the cost function calculation: the latter merely serves to remove zero-signal voxels.

For each undersampled scan and parameter map, three MAE values were computed corresponding to the three different fully sampled sequences. Presented results were based on the reference scan for which the MAE was minimal. MAE values were compared between sequences with an equal number of readouts (i.e. flip angle train length × number of repeats). A Wilcoxon signed-rank test was performed to compare MAE values of the conventionally shaped flip angle pattern, CRB optimized and undersampling optimized sequences. A p-value < 0.05 was considered to indicate a significant difference.

4 | RESULTS

4.1 | Numerical experiments

To validate the used error model and test the dependency on spatial variations in signal phase, the relative errors predicted by the model were compared to brute force validation simulations, as shown in Figure 2. Notice that the model predictions closely resemble the maps from the simulations; additionally an increasing error with larger "phase deformation" (left to right) can be observed. The T_1 error maps showed a similar outcome (see Figure S1).

Error maps for T_2 estimation, reflecting the terms from (1) before and after optimization are shown in Figure 3. Observe that the individual $\mathcal{E}_1$ and $\mathcal{E}_2$ error terms are effectively minimized and that the remaining total relative error is dominated by the PSF error (as the latter error can be mitigated only by the use of a different undersampling scheme). Also, note that the $\mathcal{E}_1$ error before optimization

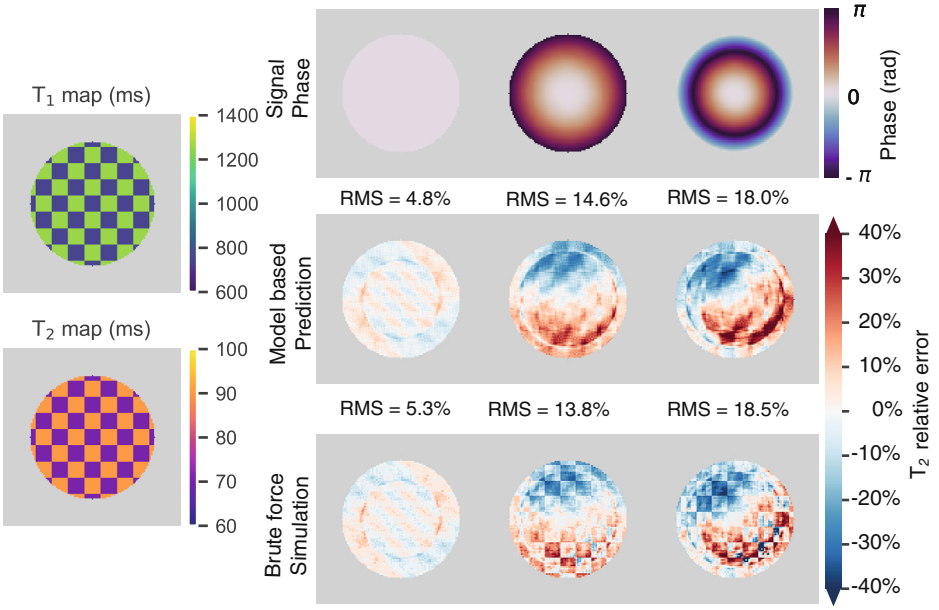

FIGURE 2 Comparison of relative errors in T_2 value predicted by the model (center row) and those obtained in brute force simulation (bottom row) for different signal phase distortions (top row). The numerical phantom with the checkerboard pattern is shown in the left column.

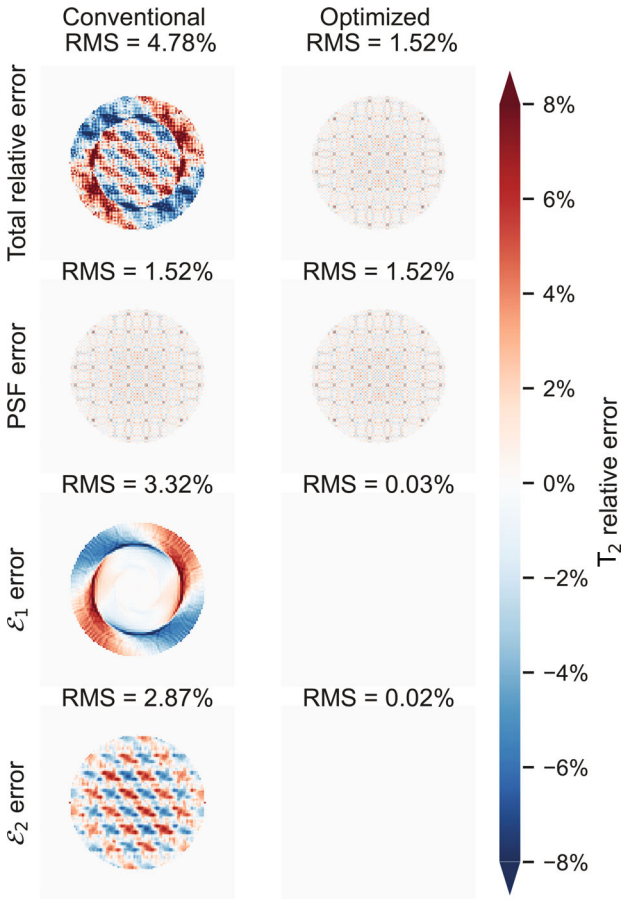

FIGURE 3 Total T_2 undersampling error estimation (upper row) subdivided into the components c.f. (1) for the numerical checkerboard phantom with a conventional and optimized flip angle pattern (left and right column respectively); the signal phase was kept spatially constant (left column in Figure 2).

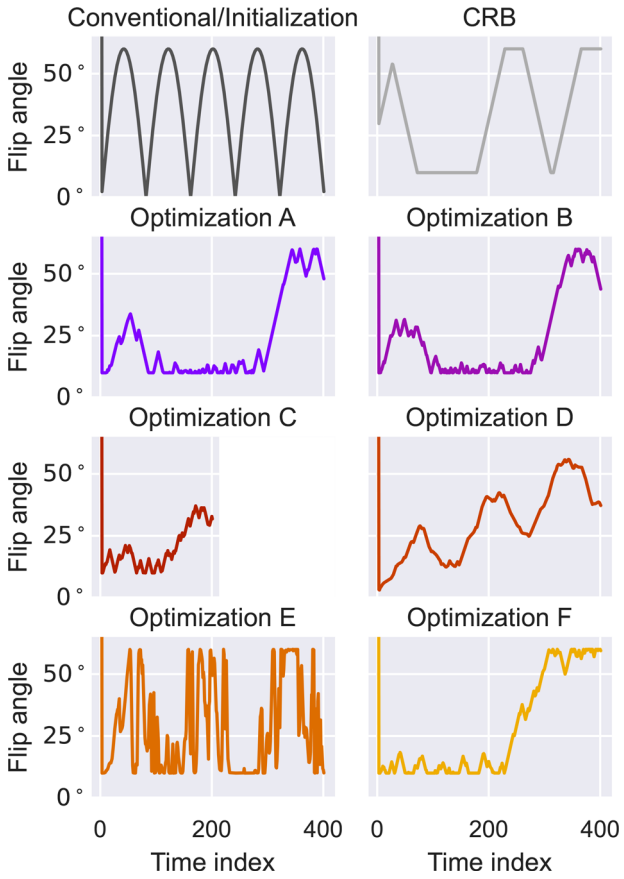

FIGURE 4 Conventional flip angle (FA) train, Cramér–Rao lower bound optimized FA train and FA trains optimized for different MR fingerprinting sequence options based on the proposed approach. The different constraints used for Optimization A to Optimization F are specified in Table 1.

does not show the spatial checkerboard-like variation, which is visible in the $\mathcal{E}_2$ error (see (1)).

4.2 | Optimization results

Figure 4 shows the conventional flip angle train, the flip angle train resulting from CRB optimization and those obtained after optimization of each sequence option with our approach using in vivo reference maps (see Figure 1). All optimized sequences begin with a 180° pulse, although this was a free parameter in the optimization. After the initial 180° pulse, each optimized sequence starts with the smallest flip angle (0° or 10°). Subsequently, they exhibit a gradual increase in flip angle (albeit varying across the sequences), except for *OptE*.

Distributions of nCRB values, per definition without taking into account undersampling artifacts, for the different flip angle trains are shown in Figure 5. These were computed for a selection of 1000 T_1 and T_2 values sampled from the reference brain (see Figure S2 for the distribution of these values). The CRB optimized flip angle pattern had the lowest combined mean nCRB (nCRB-$T_1 = 1.37 \pm 0.16$, nCRB-$T_2 = 1.69 \pm 0.19$). However, mean nCRBs of both patterns *OptA* (nCRB-$T_1 = 1.40 \pm 0.14$, nCRB-$T_2 = 1.83 \pm 0.23$) and *OptB* (nCRB-$T_1 = 1.38 \pm 0.13$, nCRB-$T_2 = 1.82 \pm 0.22$) were very similar.

4.3 | In vivo experiments

Figure 6 shows the relative error maps for one subject for sequences with 400 readouts (see Figure S3 for two other subjects). Specifically notice that the spatial correlations present with the *Conv* and CRB optimized sequence are mitigated in *OptA* and *OptD* (both regarding T_1 and T_2), and *OptC*(only for T_1). Notably, the CRB optimized pattern shows an increased error compared to all other sequences. Furthermore, the error maps for the *Conv* and CRB optimized sequence show an asymmetric distribution along

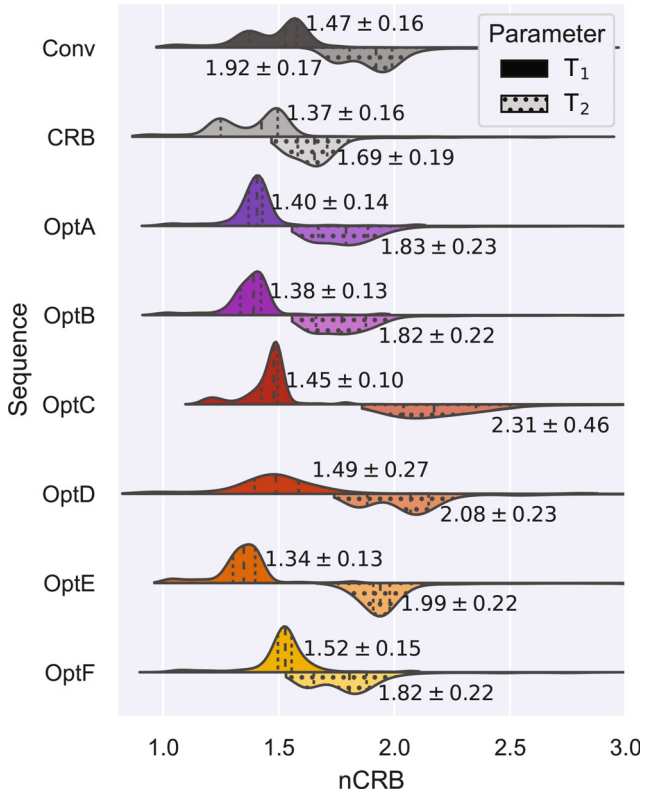

FIGURE 5 Violin plots of normalized Cramér-Rao lower bounds of T_1 and T_2 values (top and bottom of each line, respectively) for the optimized MR fingerprinting trains shown in Figure 4. Normalized Cramér–Rao lower bound values were computed for a selection of 1000 T_1 and T_2 values sampled from the reference brain in Figure 1. Values next to each distribution are the mean value and SD.

the slice. We observed in simulations that these asymmetries rotate with the starting angle of the spiral undersampling pattern, suggesting that this pattern is responsible for the asymmetric distribution.

Figure 7 shows the relative error maps for the same subject for acquisitions with 1200 readouts. Observe that the error maps show less variation for 1200 readouts than for 400 readouts, both visually and in terms of the MAE.

In Figure 8 the model-based error predictions and error maps derived from in vivo acquisitions are depicted. The figure shows results using the sequences *Conv, OptA* and *CRB*. Observe that for *Conv* and *CRB*, measured and model-based error maps show strong visual similarities and the MAE values are in agreement. However, for *OptA* the undersampling artifacts are mitigated to such an extend that other error sources become dominant in the in vivo scans resulting in a model underestimation of the MAE.

Figure 9 shows box plots of MAE values based on the scans of eight healthy volunteers. The differences between sequences were tested with the Wilcoxon test. The CRB optimized sequence differed significantly ($p < 10^{-3}$) from all other sequences, although this difference was smaller for 1200 readouts. For 400 readouts, the error in sequence *OptA*(MAE-$T_1 = 5.6\% \pm 2.87\%$ and MAE-$T_2 = 7.9\% \pm 2.31\%$) was significantly smaller than the conventional (MAE-$T_1 = 8.0\% \pm 1.92\%$, MAE-$T_2 = 14.5\% \pm 2.65\%$) and CRB optimized (MAE-$T_1 = 21.6\% \pm 4.14\%$, MAE-$T_2 = 31.4\% \pm 4.41\%$) sequences.

The differences visually observed in Figures 6 and 7 are confirmed in the MAE distributions in Figure 9. MAE values were generally smaller for the optimized sequences *OptA*-*OptD* compared to the conventional sequences. The increased number of readouts (1200) resulted in a decrease in MAE for all sequences, but the significant difference between *Conv* and *OptA* in T_2 remained. The set of optimization constraints (see Table 1) clearly affected the estimated MAE values. Sequence *OptE* (no smoothness constraint) yielded an increased error compared to *OptA* and no significant improvement compared to the *Conv* sequence. *OptF* was not optimized for T_1 and the effect of this can be seen in an increase in T_1-MAE compared to the *Conv* sequence, while the T_2-MAE is significantly smaller.

5 | DISCUSSION

We proposed an optimization scheme that mitigates the undersampling error in MRF by adjusting the flip angle train. The proposed optimization applied previously acquired parameter maps as the reference for optimization. This is the main difference with the work by Jordan et al.[9] where a numerical, discretized phantom was used, opposed to the flexibility of the here presented framework. We studied the effect of different optimization constraints and performed in vivo experiments to verify the effectiveness of our approach.

Initial numerical experiments (see Figures 2 and 3) demonstrated the effect of the signal phase on the undersampling error and how the adopted undersampling model[8] can be exploited to predict and minimize this error. The ability to correctly predict the MAE and relative error maps was further validated in in vivo scans for different sequences (Figure 8). The predicted and observed error maps were most similar when undersampling artifacts are the dominant source of error (sequences *Conv*, *CRB*). After the optimization, others error sources, such as thermal noise or misregistration, become dominant so that the error predictions do not match the in vivo results anymore (cf. sequence *OptA*).

The in vivo experiments concerned optimizations based on a single in vivo reference map (see Figure 1) while a range of constraints was applied (see Table 1). The

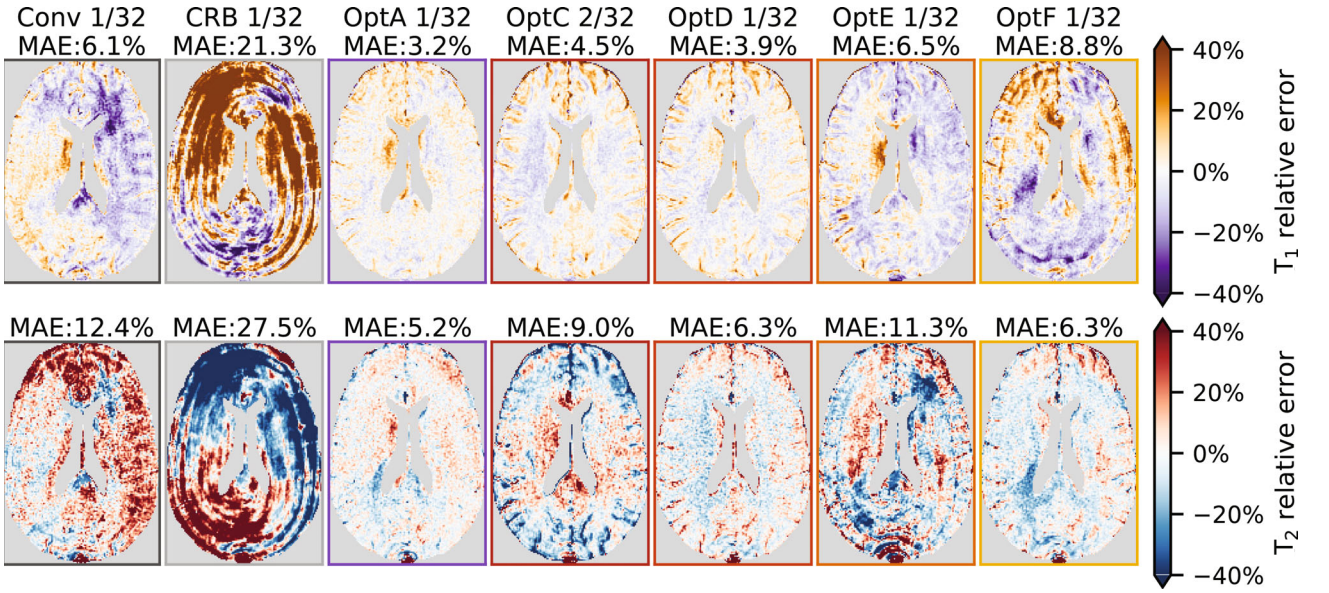

FIGURE 6 In vivo relative error maps for T_1 (top) and T_2 (bottom) in one subject, applying the different flip angle trains with 400 readouts. Above each map the corresponding Median Absolute Error (MAE) is indicated. Notice that the optimized sequences show reduced errors compared to the conventionally shaped and Cramér-Rao lower bound pattern. Observe that *OptF* was not optimized for T_1 which results in large errors in the T_1 map. The colors of the box edges correspond to the colors used in Figures 4 and 5 and reflect the different sequences.

FIGURE 7 In vivo relative error maps for T_1 (top) and T_2 (bottom) in one subject, applying the different optimized flip angle trains with 1200 readouts. Above each map the corresponding Median Absolute Error (MAE) is indicated. The colors of the box edges correspond to the colors used in Figures 4 and 5 and reflect the different sequences.

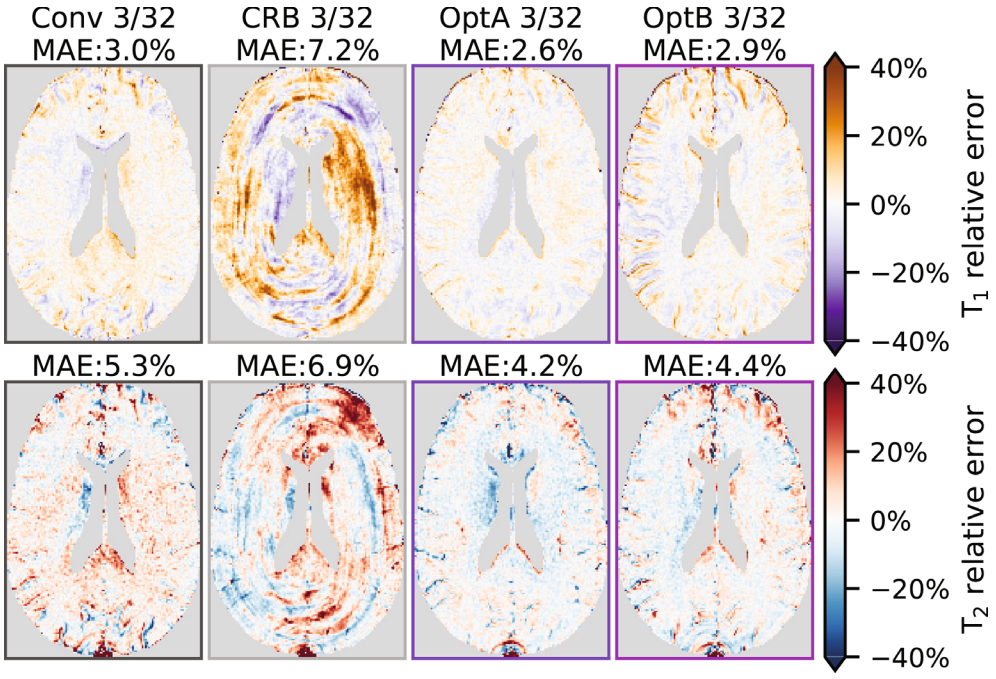

optimization showed to be effective for different parts of the brain (see Figures 9 and Figure S3), indicating that it is robust to differences between regions of interest. We only optimized and evaluated our method for T_1 and T_2 since we considered these parameters the most relevant for clinical use. The settings as used for *OptA* were chosen similar to Zhao et al.[5] Although the CRB pattern and the sequence options A-F show similarities (e.g. low FAs around index 150 and peak at the end), taking the undersampling into account in the optimization had a significant effect on the error (see Figure 9). The poor performance of the CRB optimized sequence points out that optimization for such a presumed fully sampled signal is not always effective when undersampling is used in the acquisition. The settings for *OptA* were used as a starting point for the sequence variations *OptB* to *OptF*.

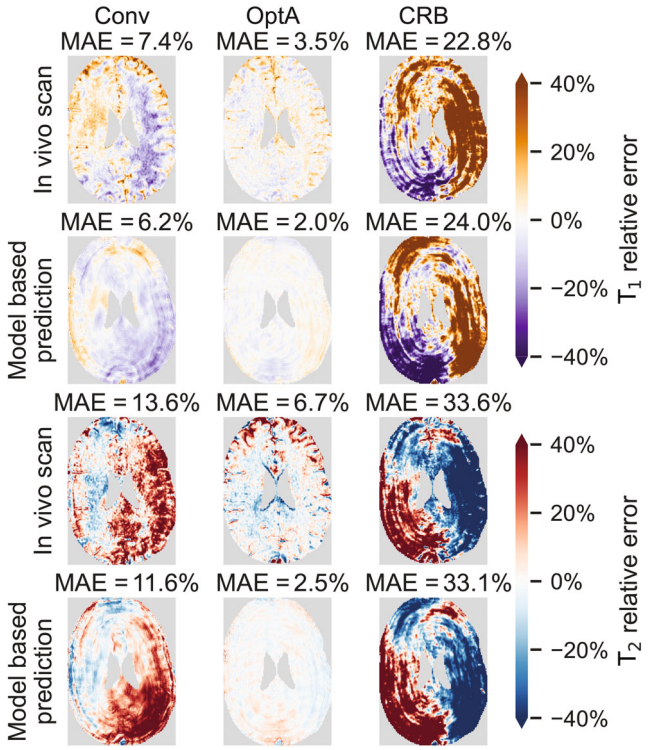

FIGURE 8 Relative error maps measured in vivo (first and third row) and model predictions (second and fourth row) for a healthy subject regarding estimation of T_1 (top two rows) and T_2 (bottom two rows) parameters for different sequences (across columns). The Median Absolute Error (MAE) was computed for the nonmasked regions.

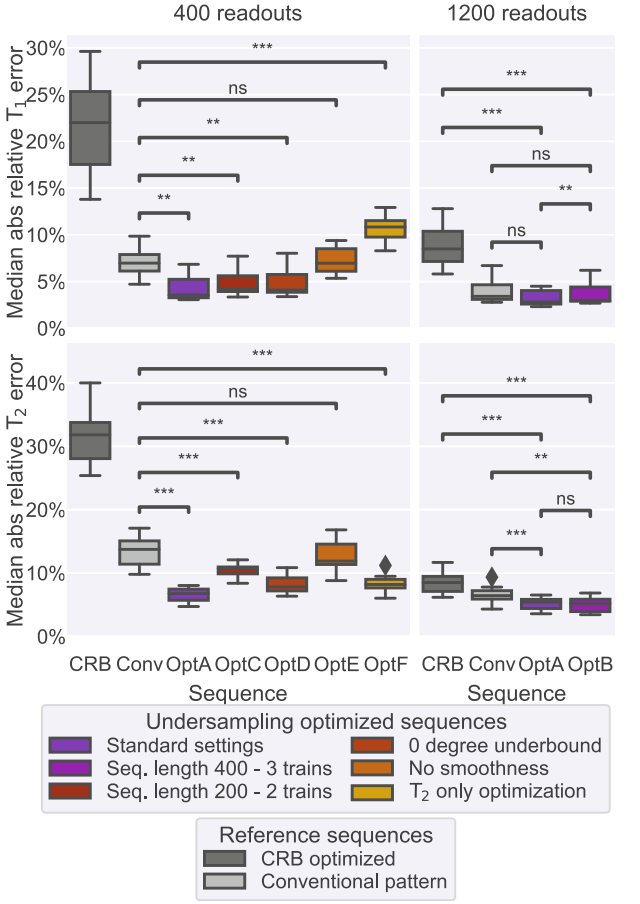

FIGURE 9 Comparison between reference sequences (gray) and sequences optimized for undersampling regarding the median absolute relative T_1 and T_2 error in scans of eight healthy subjects. Almost all sequences optimized for undersampling differ significantly from the reference sequences for the shortest scan time (400 readouts). A Wilcoxon signed-rank test was used to compare the distribution of median absolute error-values. The annotations point out noteworthy comparisons: ns indicates nonsignificance; *: $0.01 < p \leq 0.05$; **: $0.001 < p \leq 0.01$; ***: $10^{-4} < p \leq 0.001$; ****: $p < 10^{-4}$.

Sequence *OptB* was designed with three repeats of the same flip angle train, resulting in 1200 readouts. The resulting flip angle pattern only showed small differences with *OptA*. Also, the differences in MAE in the in vivo experiments were not significant. Based on this we conclude that an increased number of repetitions does not need to be taken into account in the flip angle pattern optimization.

In sequence *OptC* the sequence length was reduced to 200 flip angles and this sequence was repeated twice after a repetition delay of 6 s. As such two inversion pulses are applied, potentially enhancing T_1 sensitivity. The computed nCRBs (Figure 5) and in vivo errors (Figures 7 and 9) show that the shorter sequence length mainly affected the T_2 estimation: the nCRB increased and the T_2-MAE was significantly higher compared to *OptA*. Therefore, a longer flip angle train with less repetition (and less inversion pulses) would be preferred over a shorter sequence to improve T_2 accuracy and avoid the need of a repetition delay time of several seconds.

The lower bound of 10° was reduced to 0° for sequence *OptD* resulting in a flip angle pattern that started at 0° after the inversion pulse. The optimized sequence showed a step wise increasing pattern, which is seemingly smoother than the other patterns. Compared to *OptA* an increased T_2-nCRB was found (see Figure 5). The T_2-MAE of *OptD* showed a small increase in error compared to *OptA*, although the difference was not significant. As such both options seem viable.

Sequence *OptE* did not include a smoothness constraint, resulting in stronger variations. While reducing a potential bias, leaving out a constraint comes with an increased risk of getting trapped in a poor local minimum during optimization or overfitting. Another potential source of error is the increased sensitivity to B_1^+ inhomogeneities that is associated with a rapidly varying flip angle train.[18] This may explain the higher MAE (see Figure 9) compared to other undersampling optimized sequences

and the insignificant difference with the conventional approach.

Only optimizing for T_2 as for *OptF* yielded a high T_1-nCRB and low T_2-nCRB (see Figure 5). Simultaneously, *OptF* performed worse for T_1 than the conventional sequence, but T_2 estimations were similar to *OptA*. This indicates that the sequence improved compared to the initialization, but was not able to achieve extra T_2 sensitivity compared to combined optimization. The optimized flip angle pattern (Figure 4) shows a clear difference compared to *OptA* in the first 200 time points where all pulses stay low ($< 20°$). We hypothesize that this difference reduces the T_1 encoding and makes the sequence less appropriate for T_1 estimation.

Based on the performed experiments it may be concluded that the smoothness constraint leads to lower errors; furthermore, a longer sequence is preferred over a shorter sequence with multiple repetitions and inversion pulses (for the here considered combination of 200 and 400 flip angle pulses). The effects of reducing the lower bound on the flip angle were minimal.

The used solver (Sequential Least-Square Quadratic Programming) is prone to find different local minima, but in initial experiments we found that different initializations led to slightly different flip angle patterns with very similar cost. Potentially different optimization schemes could be applied, for example, simplicial homology global optimization,[19] to find a global optimum with respect to a certain reference map or multiple reference maps, but this would be at the cost of increased computation time. We do not consider such optimizations necessary since we do not expect the global minimum to significantly outperform the solutions we found.

A limitation of our approach is that optimizations did not include repetition time to reduce computation time. By exploiting the use of GPUs and restricting the number of free parameters, for example, using b-spline representations,[20] computation time can be further reduced to the order of minutes. This could allow for co-optimization of repetition time, and potentially further enhance the undersampling robustness of the sequence.

Computation times are also affected by the initialization choice. In particular, initialization close to the optimum will yield a reduction in computation time. A very short computation time might facilitate estimation of the optimized MRF sequences in real time. Thus, optimization could be performed based on selected scan settings, time constraints and specific geometry immediately before an actual scan.

Another limitation is that only two-dimensional acquisitions and one specific undersampling trajectory were considered. The method can be extended to three-dimensional acquisitions in a straightforward manner, although this would, again, lead to computational challenges. The optimization method can also be easily adapted to other k-space trajectories (e.g. radial or variable density spirals), where we expect that these optimizations are especially beneficial with high undersampling factors. A more complicated extension of the proposed model could be the co-optimization of the undersampling trajectory and MRF flip angle train. For such co-optimization, deep learning methods, such as supervised learning, can be of use. For example, a supervised learning framework has been proposed to design MR sequences including RF pulses and gradients for weighted images.[21]

Our paper focused on zero-filled nuFFT reconstructions and did not employ low rank reconstruction.[21,22] The use of the latter could lead to similar improvements in image quality, at the cost of increased reconstruction times. When using improved reconstructions, CRB optimized patterns may still be very effective as was shown previously.[5,6] Whether the combination of the proposed optimized sequences and more advanced reconstruction schemes can lead to further improvements or mitigates the optimization effects is another subject for further study.

6 | CONCLUSION

An optimization framework for MRF sequences taking the undersampling pattern into account was proposed and successfully validated in simulations and brain scans in healthy volunteers. The optimized flip angle patterns can mitigate the artifacts from strong undersampling in MRF. In in vivo experiments, the relative errors resulting from our optimized sequences are significantly smaller compared to standard sequence designs. The proposed framework and resulting optimized MRF sequences could be applied in further use of MRF and may reduce the need for improved reconstructions.

ACKNOWLEDGMENTS

The authors would like to thank C.C. Stolk and A. Sbrizzi for the fruitful discussions and M. Doneva, T. Amthor and P. Koken for providing the MRF patch.

FUNDING INFORMATION

This research was partly funded by the Medical Delta consortium, a collaboration between the Delft University of Technology, Leiden University, Erasmus University Rotterdam, Leiden University Medical Center and Erasmus Medical Center.

CONFLICT OF INTEREST

The authors declare no potential conflict of interests.

ORCID

David G.J. Heesterbeek https://orcid.org/0000-0002-1450-8038
Kirsten Koolstra https://orcid.org/0000-0002-7873-1511
Matthias J.P. van Osch https://orcid.org/0000-0001-7034-8959
Martin B. van Gijzen https://orcid.org/0000-0002-6491-9564
Franciscus M. Vos https://orcid.org/0000-0003-2996-6872
Martijn A. Nagtegaal https://orcid.org/0000-0002-6563-865X

REFERENCES

1. Ma D, Gulani V, Seiberlich N, et al. Magnetic resonance fingerprinting. *Nature*. 2013;495:187-192.
2. McGivney DF, Boyacíoğlu R, Jiang Y, et al. Magnetic resonance fingerprinting review part 2: technique and directions. *J Magn Reson Imaging*. 2020;51:993-1007.
3. Cohen O, Rosen MS. Algorithm comparison for schedule optimization in MR fingerprinting. *Magn Reson Imaging*. 2017;41:15-21.
4. Sommer K, Amthor T, Doneva M, Koken P, Meineke J, Börnert P. Towards predicting the encoding capability of MR fingerprinting sequences. *Magn Reson Imaging*. 2017;41:7-14.
5. Zhao B, Haldar JP, Liao C, et al. Optimal experiment design for magnetic resonance fingerprinting: Cramér-Rao bound meets spin dynamics. *IEEE Trans Med Imaging*. 2019;38:844-861.
6. Assländer J, Lattanzi R, Sodickson DK, Cloos MA. Optimized quantification of spin relaxation times in the hybrid state. *Magn Reson Med*. 2019;82:1385-1397.
7. Leitäo D, Teixeira RPAG, Price A, Uus A, Hajnal JV, Malik SJ. Efficiency analysis for quantitative MRI of T1 and T2 relaxometry methods. *Phys Med Biol*. 2021;66:15NT02.
8. Stolk CC, Sbrizzi A. Understanding the combined effect of k-space undersampling and transient states excitation in MR fingerprinting reconstructions. *IEEE Trans Med Imaging*. 2019;38:2445-2455.
9. Jordan SP, Hu S, Rozada I, et al. Automated design of pulse sequences for magnetic resonance fingerprinting using physics-inspired optimization. *Proc Natl Acad Sci*. 2021;118:e2020516118.
10. Heesterbeek DGJ. *Sequence optimisation for Magnetic Resonance Fingerprinting*. Master's thesis. Delft University of Technology Delft, The Netherlands; 2021.
11. Heesterbeek DGJ, Nagtegaal MA. MRF undersampling optimization: software and code for the publication: mitigating undersampling errors in magnetic resonance fingerprinting by sequence optimization. *4TU.ResearchData;* 2022. doi:10.4121/20101127.v2
12. Hunter JD. Matplotlib: a 2D graphics environment. *Comput Sci Eng*. 2007;9:90-95.
13. Waskom ML. seaborn: statistical data visualization. *J Open Source Softw*. 2021;6:3021.
14. Jiang Y, Ma D, Seiberlich N, Gulani V, Griswold MA. MR fingerprinting using fast imaging with steady state precession (FISP) with spiral readout. *Magn Reson Med*. 2015;74:1621-1631.
15. Hennig J. Echoes–how to generate, recognize, use or avoid them in MR-imaging sequences. Part I: fundamental and not so fundamental properties of spin echoes. *Concepts Magnet Reson*. 1991;3:125-143.
16. Kraft D. *A software package for sequential quadratic programming*. DFVLR Obersfaffeuhofen; 1988.
17. Garyfallidis E, Brett M, Amirbekian B, et al. Dipy, a library for the analysis of diffusion MRI data. *Front Neuroinform*. 2014;8:8.
18. Buonincontri G, Sawiak SJ. MR fingerprinting with simultaneous B1 estimation. *Magn Reson Med*. 2016;76:1127-1135.
19. Endres SC, Sandrock C, Focke WW. A simplicial homology algorithm for Lipschitz optimisation. *J Glob Optim*. 2018;72:181-217.
20. Scope CE, Lu H, Ye H, Wald LL, Zhao B. An efficient approach to optimal experimental design for magnetic resonance fingerprinting with B-splines. *Magn Reson Med*. 2022;88:239-253.
21. Zhao B, Setsompop K, Ye H, Cauley SF, Wald LL. Maximum likelihood reconstruction for magnetic resonance fingerprinting. *IEEE Trans Med Imaging*. 2016;35:1812-1823.
22. Assländer J, Cloos MA, Knoll F, Sodickson DK, Hennig J, Lattanzi R. Low rank alternating direction method of multipliers reconstruction for MR fingerprinting: low rank ADMM reconstruction. *Magn Reson Med*. 2018;79:83-96.

SUPPORTING INFORMATION

Additional supporting information may be found in the online version of the article at the publisher's website.

Figure S1. Comparison of the relative errors in T_1 value predicted by the model and those obtained in brute force simulation for different signal phase distortions. This figure is similar to Figure 2, but for T_1 instead of T_2.

Figure S2. Distribution of T_1 and T_2 values in the (random) selection used in CRB calculations for the inter sequence comparison of Figure 5.

Figure S3. In vivo relative error maps in two different subjects, for two different brain slices.

How to cite this article: Heesterbeek DGJ, Koolstra K, vanOsch MJP, vanGijzen MB, Vos FM, Nagtegaal MA. Mitigating undersampling errors in MR fingerprinting by sequence optimization. *Magn Reson Med*. 2022;1-12. doi: 10.1002/mrm.29554